# Formation of Bundle-Shaped β-NaYF₄ Upconversion Microtubes via Ostwald Ripening

Dangli Gao,*,† Xiangyu Zhang,‡ and Wei Gao§

†College of Science, Xi'an University of Architecture and Technology, Xi'an 710055, P. R. China
‡Electronic Materials Research Laboratory (EMRL), Xi'an Jiaotong University, Xi'an 710049, P. R. China
§College of Physics and Information Technology, Shaanxi Normal University, Xi'an 710062, P. R. China

Ⓢ Supporting Information

**ABSTRACT:** In this work, the uniform bundle-shaped microtubes composed of six half-pipes are synthesized for the first time in hydrothermal solutions via an intentional delayed phase transition pathway induced by $Mn^{2+}$ doping. The structural and kinetic factors that govern the phase and shape evolution of $NaYF_4$ microcrystals have been carefully studied, and the influences of $Mn^{2+}$ to $RE^{3+}$ ratio, the amount of trisodium citrate, and the pH value in conjunction with the intrinsic character of $RE^{3+}$ ions on the phase and shape evolution are systematically discussed. It is found that the proper $Mn^{2+}$ to $RE^{3+}$ ratio is mainly responsible for delayed phase transition process and induces interior density gradient of solid aggregate for creating hollow bundle-shaped microtubes. While the amount of trisodium citrate and the pH value are the keys for the shape control of the $NaYF_4$ microcrystals such as prismatic microtubes, prismatic short rods, thin plates, and particles. The up and downconversion emissions were obtained independent of whether $\alpha$- or $\beta$-$NaYF_4$:$Er^{3+}$/$Yb^{3+}$ samples doped with $Mn^{2+}$, but the significant tuning of output color was only obtained in cube $NaYF_4$ nanoparticles rather than in hexagonal microtubes via adjusting the amount of $Mn^{2+}$ ions. These spectral measurements and EDX analyses indicate that the distribution or concentration of $Mn^{2+}$ in hexagonal phase solid solution has changed, which supports Ostwald ripening growth mechanism and rules out agglomeration or oriented attachment growth mechanism. We designed crystal growth mode by simply addition of dopant may provide a versatile approach for fabricating a wide range of hollow nano/microcrystals and thus bring us a clearer understanding on the interaction between the dopant reagents and the nano/microcrystals.

**KEYWORDS:** bundle-shaped microtubes, hydrothermal approach, delayed phase transition, Ostwald ripening, upconversion luminescence
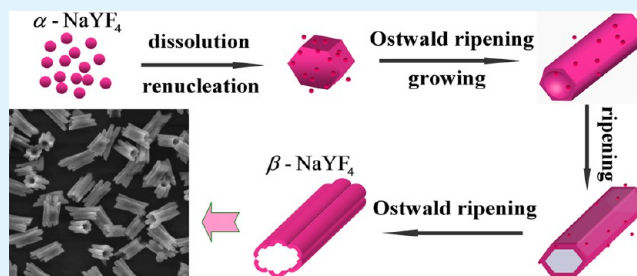
## ■ INTRODUCTION

Recently, the development in the synthesis of colloidal nano/microcrystals with interior hollow structures has aroused considerable attention due to the potential applications in encapsulation, ion exchange, drug delivery, optics, and catalysts.[1−5] A variety of conventional solution-synthetic methods have been used for the preparation of such structures, most of which are synthesized in the presence of either hard templates or soft directing agents by multistep procedures. To circumvent these difficulties, two template-free technologies, involving Ostwald ripening[6,7] and Kirkendall effect,[1−4] have been used to prepare a large variety of hollow materials, such as $Cu_2O$, $SnO_2$, and $Co(OH)_2$.[8−10] Among them, mass transport via Ostwald ripening has been proven to be a facile approach to generate symmetric and/or asymmetric interior spaces for inorganic nano/microstructures. However, it should be mentioned that, at the present stage of development, it is only limited to simple monometallic oxides, hydroxides, sulfides, or stoichiometric transition-metal tetraoxometalates.[8−12] Simple and one-step template-free synthetic method

is only used for the preparation of some specific hollow materials and serious lack of artificial design. It still remains a major challenge for synthesizing hollow-structured nano/microstructures with designed chemical compositions and controlled morphologies.

As an important category of functional materials, rare earth (RE) fluorides have attracted much research interest due to their potential applications in optical telecommunication,[13] catalysts,[14] biochemical probes,[15] and medical diagnostics[16,17] based on their unique properties arising from the transitions of 4f electrons. Among the various RE fluorides, $NaYF_4$ has been regarded as currently the most excellent host lattices for RE ions due to many advantageous features such as low vibrational energy and good optical transparency over a wide wavelength range.[18] Therefore, different morphologies of $NaYF_4$ crystals, including nano/microspheres,[19] nano/microrods,[20] nanostruc-

tured arrays,[21] hexagonal ($\beta$) prisms,[22] nano/microtubes,[23,24] nano/microdisks,[25,26] polygonal columns, and hexagonal tablets,[27] the core/hollow/shell structures and hollow/shell structures,[5] based on different solution-based routes have been prepared. The well-known physical phenomenon Ostwald ripening, which involves the growth of larger crystals from those of smaller size, has been widely employed in template-free fabrication of hollow inorganic nano/microstructures in recent years. Nevertheless, the approach has still not been used intentionally for the preparation of hollow $NaYF_4$ structures.

Recently, impurity doping is found to have great impact on the growth of many functional materials. For instance, Liu's group[20] and Wang's group[28] demonstrated phase transformation from cube ($\alpha$) to hexagonal phase of $NaYF_4$ nanocrystals by doping $RE^{3+}$ ions with large ionic radius. $Ti^{4+}$ doping-induced cubic-to-hexagonal $NaYF_4$ phase transition at low temperature (down to 130 °C) in a liquid−solid−solution reaction system was investigated by Chen and co-workers.[29] While the reverse process from $\beta$-$NaYF_4$ phase to $\alpha$-phase is implemented by doping $Mn^{2+}$ with small ionic radius.[30] Despite these efforts, the dynamic process controlled by dopant and interactions between dopant ions and host lattices during the growth of doped nanocrystals are not fully understood. It should be noted that either interstitials or vacancies are usually formed, when the ions with different valences are doped.[31] Cation exchange may be also induced by dopant ions in a solution reaction system.[32] In addition, interparticle interactions are stronger at initial stage of the growth for primary ultrasmall particles due to Brownian motion and diffusion.[33−35] Because of the complexity of the crystal structures, compositions, and interactions, it is still a difficult challenge to clearly identify the critical role of dopant in determining the structure and growth process of crystals, which may be the key in developing a novel method for the controlled growth of nanocrystals. In addition, to the best of our knowledge, no investigation exists on how the dopant ions in precursor solution influences the phase transition process of primary particles and growth process of the final product particles such as Ostwald ripening process.

Applicability of Ostwald ripening methods for synthesizing hollow-structure materials must widen urgently to RE fluorides systems. In this Article, we synthesized uniform bundle-shaped $NaYF_4$ hollow microtubes composed of six half-pipes by Ostwald ripening, caused by doping $Mn^{2+}$. The $Mn^{2+}$ ions, with smaller ionic diameter than $Y^{3+}$, are carefully chosen to control phase transition and create interior density gradient of solid aggregate. The architecture of the void space becomes possible upon Ostwald ripening process driven by the particle-density gradient. In addition, tunable upconversion emissions of products via back energy transfer between $Er^{3+}$ and $Mn^{2+}$ ions were investigated in detail.

## ■ EXPERIMENTAL SECTION

**Chemicals.** The RE oxides $Y_2O_3$ (99.99%), $Yb_2O_3$ (99.99%), and $Er_2O_3$ (99.9%) were purchased from Sinopharm Chemical Reagent Co., Ltd, China, and other chemicals were purchased from Beijing Fine Chemical Company, China. All chemicals are of analytical grade reagents and used directly without further purification. RE nitrate stock solutions of 0.2 mol/L were prepared by dissolving the corresponding metal oxide in nitric acid at elevated temperature.

**Sample Preparation.** $NaYF_4$ microcrystals have been fabricated via a facile hydrothermal route assisted with trisodium citrate.[22] In a typical procedure, 1.5 mL of trisodium citrate (0.4 mol/L) was added to a mixture containing 0.6 mmol of RE nitrate (3.0 mL of 0.2 mol/L

$RE(NO_3)_3$, RE = Y, Yb, and Er) and 20 mL of deionized water. The solution was then thoroughly stirred for 30 min to form a chelated RE citrate complex (1:1 molar ratio for $Cit^{3-}$/$RE^{3+}$). Then, 6 mL (1.0 mol/L) of $NH_4F$ aqueous solutions were dropped into chelated RE citrate complex under thoroughly stirring. The pH value of the mixture was tuned with ammonia water or nitric acid solution. Subsequently, the milky colloidal solution was transferred to a 40.0 mL Teflon-lined autoclave, and heated at 200 °C for 24 h. The final product was collected by centrifuging and washed with water and ethanol. The collected microcrystals were dried under 60 °C for 12 h. In addition, RE fluoride prepared with 2:1 and 5:1 molar ratios of citrate ions to RE ions ($Cit^{3-}$/$RE^{3+}$) were prepared with stoichiometric 1 mol/L of trisodium citrate, and other conditions are the same as those mentioned above for synthesizing $NaYF_4$ (1:1 molar ratio for $Cit^{3-}$/$RE^{3+}$).

In a typical control experiment procedure, $NaYF_4$:$Yb^{3+}$/$Er^{3+}$precursor particles, obtained after heating at 200 °C for 2 h, were redispersed in a solution mixture consisting of a certain amount of trisodium citrate, $NH_4F$ and $Mn^{2+}$. The mixed solution was transferred to a 40.0 mL Teflon-lined autoclave after stirring for 1 h, and heated at 200 °C for 20 h. The final product was collected by centrifuging and washed with water and ethanol. The collected microcrystals were dried under 60 °C for 12 h.

**Characterization.** Powder X-ray diffraction (XRD) measurements were performed on a D/Max2550VB+/PC X-ray diffraction meter at a scanning rate of 15°/min in the $2\theta$ range from 15° to 75°, with Cu Ka (40 kV, 40 mA) irradiation ($\lambda$ = 0.15406 nm). Scanning electron microscopy (SEM) micrographs were obtained using a Hitachi S-4800 FE-SEM. An energy dispersive X-ray spectroscopy (EDX) facility attached to the FEI Quanta 200 environment SEM was employed to analyze the chemical composition. A Ti: sapphire continuum laser (MBR-110) and a 532 nm YAG:$Nd^{3+}$ pulsed laser (Quanta Ray Lab-170) were employed as upconversion and downconversion excitation sources, respectively. The monochromator (SP 2750i) with a spectral resolution of approximately 0.008 nm and a charge coupled device (ACTON, PIXIS 100) was used for luminescence collection and detection. The corresponding notch filters were placed in front of the entrance of the monochromator to block the scattering light. All the measurements were performed at room temperature.

## ■ RESULTS AND DISCUSSION

The bundle-shaped $NaYF_4$:$Er^{3+}$ hollow microtubes have been synthesized by the modified hydrothermal strategy in the presence of 30% $Mn^{2+}$ dopant under basic conditions.[22] The microtubes are uniformly composed of six half-tubes with outer diameters of about 6 um and lengths of about 12 $\mu$m, as shown by SEM in Figure 1a. EDX of the 30 mol % $Mn^{2+}$-doped $NaYF_4$:Er microcrystals as a precursor reveals the existence of the doping element $Mn^{2+}$ (Figure 1b). XRD patterns further indicate that the microtubes obtained consist of pure $\beta$-$NaYF_4$ (Figure 1c). No obvious extra diffraction peaks were detected even the $Mn^{2+}$ ions concentration up to 30 mol %, indicating the formation of a Y−Mn solid solution. In addition, the diffraction peak shifts slightly to the higher-angle side as a result of decreasing the unit-cell volume due to the substitution of $Y^{3+}$ ions by smaller $Mn^{2+}$ ions in the host lattice (Figure 1c).[30] To the best of our knowledge, this kind of bundle-shaped $NaYF_4$:$Er^{3+}$ hollow microtubes is synthesized for the first time.

The controlled experiments were carried out to explore the mechanism of the formation of the bundle-shaped microtubes. Figure 2 shows the morphology transformation and size evolution of a series of $NaYF_4$ microcrystals doped with different amount of $Mn^{2+}$. The XRD patterns demonstrate that all the products obtained remain the same $\beta$-phase $NaYF_4$ structures (Figure S1 in the Supporting Information). SEM images reveal that the products without $Mn^{2+}$ doping are prismatic microtubes with a broad particle size distribution
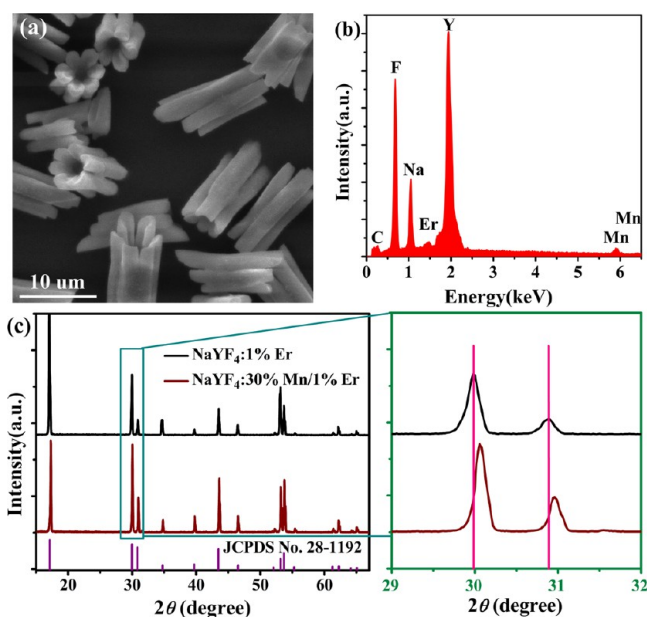
**Figure 1.** (a) SEM image and (b) EDX spectrum for 30 mol % $Mn^{2+}$ ions doped $NaYF_4$:$Er^{3+}$ (2 mol %) microcrystals. (c) XRD patterns for two $NaYF_4$:$Er^{3+}$ (2 mol %) microcrystals in the presence of 0 and 30 mol % $Mn^{2+}$ dopant ions.
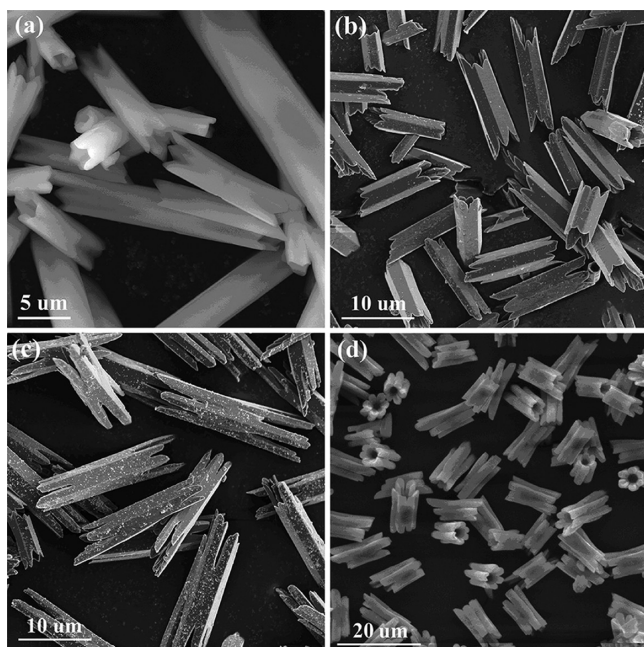


**Figure 2.** SEM characterization of $NaYF_4$: $Er^{3+}$(1.0 mol %) microcrystals obtained after heating for 24 h at 200 °C in the presence of (a) 0, (b) 10, (c) 20, and (d) 30 mol % $Mn^{2+}$ dopant ions.

(Figure 2a). The diameters and lengths of these microtubes are about 4−8 and 10−18 $\mu$m, respectively. It is noted that the outside surfaces of these prismatic microtubes are composed of six lateral planes with a reentrant groove and two crown-like shapes on top end surfaces. Obviously, the crown-like top ends are in good agreement with lateral planes with reentrant grooves. Yielding microtubes with a very narrow particle size distribution are only obtained after doping $Mn^{2+}$ ions (Figure 2b−d). With the addition of $Mn^{2+}$ ions, the tubal walls become gradually thin until the lateral planes split at reentrant grooves.

Further increasing the doped amount of $Mn^{2+}$ to 30%, the six lateral planes were completely splitted at reentrant grooves and curled to arris leading to fairly uniform bundle-shaped $NaYF_4$:$Er^{3+}$ hollow microtubes composed of uniformly six half-pipes (Figure 2d). These results indicate that the $Mn^{2+}$-doping influences the growth dynamics process to give simultaneous control of morphology and size of the microtubes. By rational controlling the $Mn^{2+}$-doping level, fairly uniform bundle-shaped $NaYF_4$:$Er^{3+}$ hollow microtubes can be obtained.

To shed light on the shape evolution of $Mn^{2+}$ doped bundle-shaped $NaYF_4$ microtubes, detailed time-dependent experiments were carried out under the ratio of $Cit^{3-}$/$RE^{3+}$ of 1:1 and pH value of 8.5. Figure 3 is a series of SEM images showing morphological evolution of the fluoride microtubes. With a short reaction time (2−8 h), the crystallite aggregates give a roughly spherical morphology (Figure 3a and b). When the reaction time prolonged to 10 h, the hexagonal $NaYF_4$ microplates with concave top end facets are formed (Figure 3c). After 13 h of reaction, the hexagonal $NaYF_4$ crystallite aggregates were solid microrods with wedge-shaped instead of channel structures and some irregular spherical aggregates (Figure 3d). The mixtures present a fairly broad particle size distribution. At the same, it is noted that the solid evacuation did take place, but only for certain regions such as at up/down surface of individual rods. After 18 h of reaction, the microrods gradually become uniform and completely translate to microtubes, but a few solid spherical small particles still essentially can be observed (Figure 3e). These microtubes are composed of six smooth lateral planes with reentrant grooves. The average diameter and length are around 6 and 14 $\mu$m, respectively. Quite interestingly, with a longer reaction time of 24 h, the formed hollow microtubes, composed with six half-pipes, are quite uniform with a 100% morphological yield (Figure 3f). The shapes of the microtubes are different from the counterparts with the reaction time of 18 h, but the average sizes almost keep the same. The fairly uniform bundle-shaped $NaYF_4$:$Er^{3+}$ structures composed of uniformly six half-pipes enable them to serve as novel building blocks for new device applications.

The XRD patterns of the intermediates obtained at different reaction time intervals are shown in Figure 4. They reveal that the intermediates display distinctively different XRD patterns at different reaction periods. The hydrothermal treatment for 2−8 h leads to the formation of a pure cubic $NaYF_4$ phase (JCPDS No. 06-0342) in Figure 4a−c. With the reaction proceeding for 13 h, a dissolution−renucleation process for nanospheres takes place, and the more stable crystalline phase, namely, hexagonal $NaYF_4$, emerges (Figure 4d). But the diffraction peaks of the samples cannot be indexed as a pure hexagonal phase until the reaction time is extended to 24 h (Figure 4d−f).

The integration of XRD patterns and the corresponding SEM images of the different intermediate samples doped with $Mn^{2+}$ at different reaction stages clearly indicates that $NaMnYF_4$ products undergo an $\alpha \to \beta$ phase transformation coupled with a morphology evolution. An evolution mechanism is proposed based on a delayed phase transition induced by $Mn^{2+}$ doping as shown in Scheme 1. At a short reaction time (2−8 h), numerous small metal fluoride crystallites nucleate from solution under hydrothermal conditions and quickly congregate to cube phase spherical nanoparticles in order to reduce the surface energy. The small cube phase nanoparticles are metastable relative to the equivalent bulk material due to
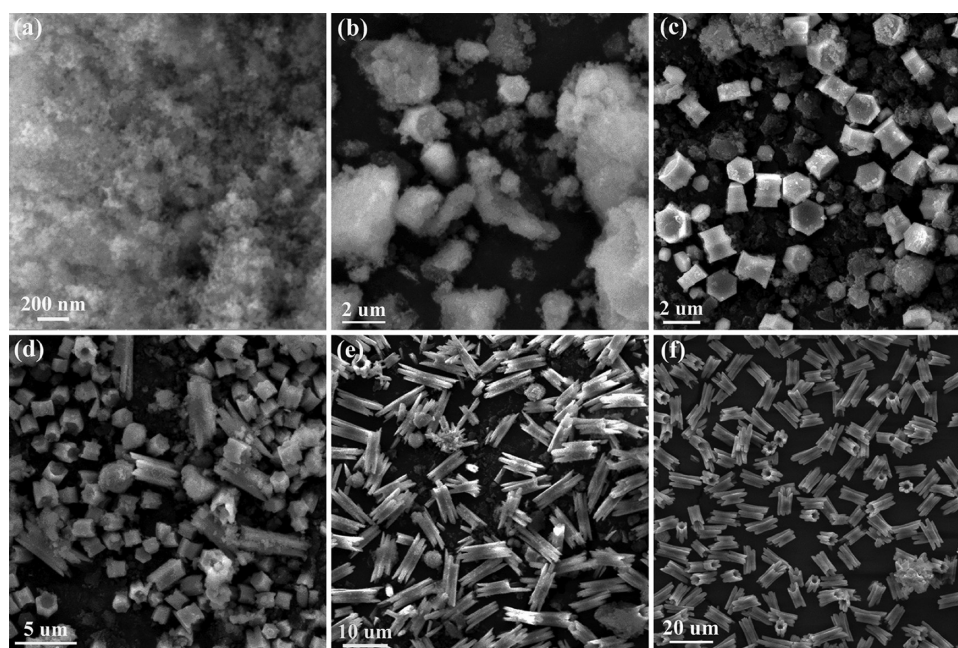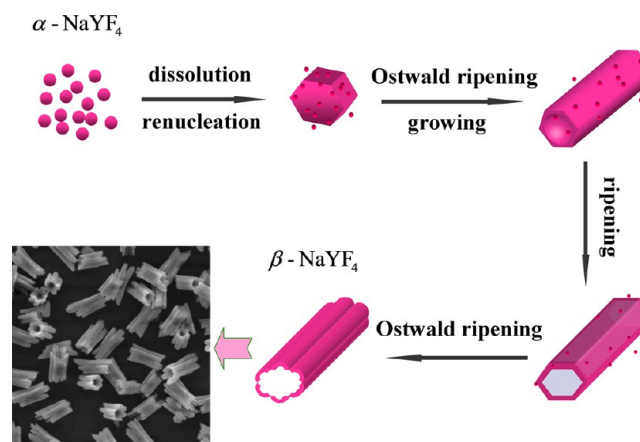
**Figure 3.** SEM patterns for NaYF$_4$: Er$^{3+}$(1.0 mol %) samples obtained in the presence of 30 mol % Mn$^{2+}$ dopant ions as a function of hydrothermal reaction time. The reaction time is (a) 2 h, (b) 8 h, (c) 10 h, (d) 13h, (e) 18 h, and (f) 24 h.
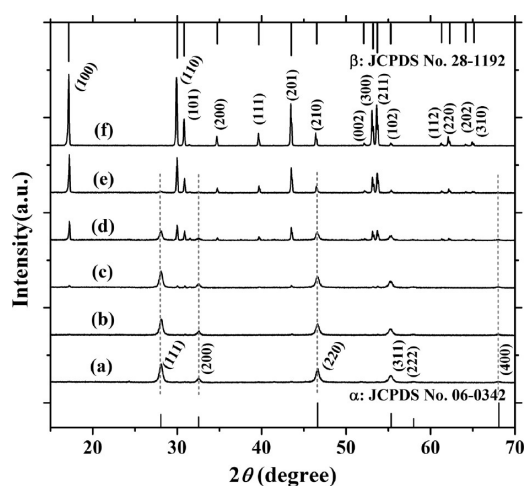


**Figure 4.** XRD patterns of 30 mol % Mn$^{2+}$ doped NaYF$_4$: Er$^{3+}$(1.0 mol %) microcrystals prepared by different hydrothermal reaction time at 200 °C: (a) 2 h, (b) 4 h, (c) 8 h, (d) 13 h, (e) 18 h, and (f) 24 h.

**Scheme 1. Schematic Illustration of the Possible Formation Processes of the $\beta$-NaYF$_4$ Microtubes with Six Half-Pipes**



the thermodynamic tendency for growth. Previous reports have demonstrated that the size of the substitutional dopant ions plays a key role in stabilizing a specific crystalline phase in the NaYF$_4$ based hybrid materials.[20,30,31] In addition to, the substitution ions with larger ionic radius favor the hexagonal structures, whereas the smaller substitution ions tend to produce the cubic phase of the final products. In our present case, the Mn$^{2+}$ ions ($r$ = 0.81 Å) with a smaller size than Y$^{3+}$ ($r$ = 0.89 Å)[30] were introduced into NaYF$_4$ host as a stabilizer to keep cube phase, which is supported by the presence of few cube phase particles after reaction for 18 h. The delayed phase transformation process, induced by doping Mn$^{2+}$, leads to a bigger size of the initial particles and a exhausting of the active monomer species (molecular educts) in the precursor solution. The $\alpha$ phase nanoparticles seem not to be of the equilibrium state when the physical dimension of the initial particle increases to critical size of the phase transition from cubic to hexagonal.[21] With the reaction time further prolonged, anisotropic growth becomes dominating by rapid dissolving of $\alpha$-particles and releasing of monomers, resulting in a sudden nucleation of $\beta$-NaYF$_4$. Charge balance was disturbed by doping divalent Mn$^{2+}$ ions.[36,37] To maintain charge balance, the defects of F$^-$ vacancies and Na$^+$ interstitials are formed during the nucleation stage, which breaks the perfect symmetry of crystal lattices and enhance anisotropic growth of the starting nuclei. Thereafter, the size evolution of the $\beta$-phase particles shows two distinctly different stages. In the first stage, the $\beta$-phase particles grow very fast, while the molar fraction of precursor $\alpha$-particles rapidly dissolves as the single provider of monomers (Figure 3c−e). Noted that molecular educts in the solution have been almost depleted in $\beta$-phase particles grow process due to the delay of phase transition. In the second stage, most of the $\alpha$-phase particles have already been consumed and the growth rate of the $\beta$-phase particles is slower (Figure 3e and f). Note that as long as their molar

fraction is not too low, the $\alpha$-phase particles still increase in size.

Since the rate constant of the reaction between particles and monomers is expected to vary monotonically with size,[38] the fast growth rate in the first stage must be connected to the high amount of monomers released during the fast dissolution of the $\alpha$-phase particles. The $\alpha$-phase particle is considered as single precursor due to depletion of molecular educts in the solution by delaying phase transition. The $\beta$-phase seeds consumed the vicinal monomers formed the initial hexagonal prism, so that the concentration of monomers near $\beta$-phase particles decreases and the near $\alpha$-phase particles accelerate dissolution as a supplement. The released monomers meet the extending top corner and lateral ribs of initial hexagonal prism firstly, leading the accelerated growth rate of the top corners and lateral ribs and finally to form a microrod composed of bulgy edges, lateral planes with reentrant grooves and crown-like top ends (Figure 3c). The growth process is much like the growth process of $NaYF_4$ nanocrystals by using $\alpha$-phase particle as single precursor.[39] The $\alpha$-phase particles therefore seem to act as a homogeneously dispersed reservoir of monomers.[40] The growth rate of the $\beta$-particles controlled by the diffusion rate of monomers will present downward trend. If such a reservoir releases monomers at a rate sufficient to ensure a moderate to high level of supersaturation during the first stage of the $\beta$-particles growth, focusing of sizes by diffusion-control will occur in accord with the observed narrow particle size distribution of final products.[34,40,41] Since the $\alpha$-phase is thermodynamically less stable than the $\beta$-phase, the $\alpha$-phase particles finally are depleted and $\beta$-phase particles complete the focusing of the size. However, the $\beta$-phase hexagonal prisms Y—Mn solid solution particles are weak crystalline due to a rapid grow rate in the first region and the doping of $Mn^{2+}$ ions. Furthermore, introducing the $Mn^{2+}$ ions into $\beta$-$NaYF_4$ hosts, $F^-$ vacancies and $Na^+$ interstitial ions can also be coupled into the crystalline process creating weak crystalline solids. The inner crystallites of the initial hexagonal prisms might be weaker than that of outer owing to the decline in grow rate, which make crystallites dissolve and transfer out, producing a wedge-shaped instead of channel structures connecting inner space and outer space. Crystallites relocation during prolonged processes, which is indispensable in the ripening, may also result in unexpected hollow structure if starting solid precursors become compositionally complicated. Many ionic dopants in different valence states have been investigated, including both metallic ions and nonmetallic ions in order to induce the Ostwald ripening process or Kirkendall effect.[42−44] When the reaction time is further extended to 24 h, we believe that even the microtube structures are already in the hydrodynamic stable $\beta$-phase, the inner crystallites of the hexagonal prism microtubes could still diffuse outward to the shell via the Ostwald ripening and then change the degree of crystallinity of the $NaYF_4$ microcrystals. The middle mass go on transferring out till lateral planes split from reentrant grooves. Subsequently, lateral planes roll to arris in order to reduce surface energy forming six half-pipes. It can be seen that the molar ratio of $Mn^{2+}/RE^{3+}$ and reaction time are two key factors that affect the shape of $\beta$-$NaYF_4$ microcrystals. The shape evolution schematic of bundle-shaped microtubes was shown in Scheme 1.

Compared to the standard synthesis of bundle-shaped microtubes, the growth conditions were simplified by using small purified particles of $\alpha$-$NaYF_4$ as single-source precursors reacting with $Mn^{2+}$ under hydrothermal condition to further confirm the role of $Mn^{2+}$ in the synthesis process of bundle-shaped microtubes. Figure S2 displays images of SEM and XRD for the initial $\alpha$-phase and the resulting $\beta$-phase product particles. When $\alpha$-phase precursor particles react with $Mn^{2+}$ ions under hydrothermal condition, similar bundle-shaped microtubes accompanying with microrods with concave-like top end can be observed in Figure S2. In addition to, a broad particle size distribution for $\beta$-phase product particles is present, which may result from the fast depletion of $\alpha$-phase particles and initial Ostwald ripening process between $\beta$-phase particles. These results indicate that the influence of $Mn^{2+}$ ions on the growth of the bundle-shaped $NaYF_4$ microtubes may lie in three aspects: (i) Delaying phase transition of the $\alpha$-phase particles to act as single monomer supply. (ii) Preventing Ostwald ripening process between $\beta$-phase particles to achieve the focus of the size of $\beta$-phase particles. (iii) Creating interior density gradient of solid aggregate by forming defects to induce Ostwald ripening process in single $\beta$-phase particles. The controlled experiment further supports the shape evolution mechanism of bundle-shaped microtubes proposed in Scheme 1.

Citrate is an important biological ligand which can adsorb strongly on metal and mineral surfaces and significantly alter the surface properties and mineral growth behavior.[30,45] XRD patterns of the samples prepared under various molar ratio of $Cit^{3-}/RE^{3+}$ conditions of (a) 1/1, (b) 2/1, and (c) 5/1 are presented in Figure S3. As shown in Figure S3, it is found that the fluoride products obtained under different molar ratios of $Cit^{3-}/RE^{3+}$ conditions adopt the same pure hexagonal phase structures. In addition to, there is a modification on the relative intensities of (110) peak to (101) peak on XRD patterns of these samples, indicating a modification on the preferential growth orientation, which is consistent with previous report.[46] The SEM images reveal that fairly uniform bundle-shaped $NaYF_4$ microtubes, short prismatic with the crown-like top end surfaces and thin microplates can be obtained by increasing the amount of trisodium citrate to different extent, respectively (Figure S4). It has been suggested that citrate ions may bind on the (001) plane and exert strong inhibiting effects on ZnO elongation.[45] We believe that a similar effect occurs during our synthesis process. The crystal growth is remarkably restricted along the [0001] direction by the increase of the amount of the $Cit^{3-}$ leading to thin plate. Further investigations revealed that the molar ratio of $Cit^{3-}/RE^{3+}$ is the dominant parameter for controlling the shape of $NaYF_4$: $Mn^{2+}/Er^{3+}$ microcrystals.

It is reported that pH of the solution not only can tune the crystal structure,[2] but also induce the different selective adsorption ability of $Cit^{3-}$ anions on the different crystal facets,[46] and subsequently alter the surface properties and mineral growth behavior. At a fixed hydrothermal parameter but changing the pH value of the mother liquid from 6 to 10, all XRD measurements show a pure hexagonal phase as presented in Figure S5. The effect of pH on the ratio of the relative intensities of (110) peak to (100) peak in the XRD patterns is similar as the effect of the ratios of $Cit^{3-}/RE^{3+}$, which indicates that pH can modify selective adsorption ability of $Cit^{3-}$ anions.[46] SEM images shown in Figure S6 reveal that uniform bundle-shaped $NaYF_4$ microtubes can be obtained by tuning the pH value of mother liquid to 8.5.

Moreover, we found that the radius of matrix ions also had a complicated effect on the resultant crystal morphology. Similar hollow structures are also obtained for the other RE ions such as hollow $NaYbF_4$ microtubes as given in Figure S7. But evident

9736

dx.doi.org/10.1021/am402843h | ACS Appl. Mater. Interfaces 2013, 5, 9732−9739

hollow structures created by the Ostwald ripening process depend on the ratio of the radius of $Mn^{2+}$ to matrix $RE^{3+}$. The Ostwald ripening process can be slowed down by doping $Mn^{2+}$ with the similar radius as $Yb^{3+}$ in $NaYbF_4$ microcrystals leading to the smaller hollow pipe diameter.

To investigate the upconversion luminescence properties of a series of $Mn^{2+}$ doped fluoride products including cube $NaYF_4$ nanoparticles, hexagonal $NaYF_4$ microtubes and hexagonal $NaYbF_4$ hollow microrods, $Yb^{3+}/Er^{3+}$ ion pair is codoped into fluoride host materials. It is noted that doping with 18% $Yb^{3+}$/ 2% $Er^{3+}$ (molar ratio) alters neither the crystal structure nor the morphology of the hexagonal $NaYF_4$ microtubes when reaction time is extended to 30 h (Figures S7 and S8). Under 980 nm laser excitation, the room-temperature upconversion emission spectra for a series of samples are presented in Figure 5. It can
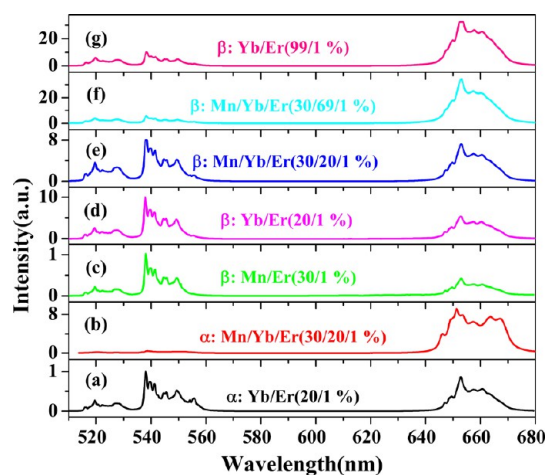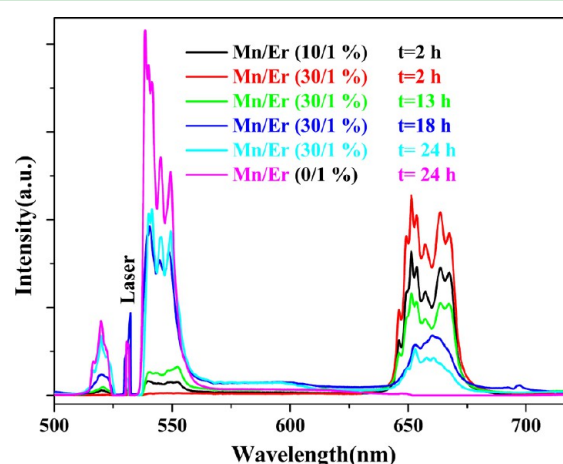


**Figure 5.** Upconversion emission spectra of (a) $\alpha$-$NaYF_4$:Yb/Er(20/1 mol %), (b) $\alpha$-$NaYF_4$:Mn/Yb/Er(30/20/1 mol %), (c) $\beta$-$NaYF_4$:Mn/ Er(30/1 mol %), (d) $\beta$-$NaYF_4$:Yb/Er(20/1 mol %), (e) $\beta$-$NaYF_4$:Mn/ Yb/Er(30/20/1 mol %), (f) $\beta$-$NaYF_4$:Mn/Yb/Er(30/69/1 mol %), and (g) $\beta$-$NaYbF_4$:Er(1 mol %). All the samples are measured under the same conditions with 980 nm laser as the excitation source operating at 360 mW.

be seen clearly that, in all seven samples, the emission spectra are similar in shape, namely, they exhibit three obvious emission bands centered at 521, 539, and 654 nm that are assigned to $^2H_{11/2} \rightarrow ^4I_{15/2}$, $^4S_{3/2} \rightarrow ^4I_{15/2}$, and $^4F_{9/2} \rightarrow ^4I_{15/2}$ transitions of $Er^{3+}$, respectively.[25,47−51] Part of the *f*-electronic levels for the $Yb^{3+}$, $Er^{3+}$, as well as $Mn^{2+}$ along with main transitions and proposed upconversion mechanism are indicated in Figure S9.[30,52]

Zhao and co-workers demonstrated that doping $Mn^{2+}$ ions into $NaYF_4$: Yb/Er can tune the red to green intensity ratio and promote the transition of red emission of $NaYF_4$ nanocrystal because of the energy transfer between the $Er^{3+}$ and $Mn^{2+}$.[30] The similar experiment phenomenons in Yb/Er co-doped $MnF_2$ and $NaMnF_3$ nanoparticles have been reported.[37,53] Even, Liu *et al.* reported single-band upconversion emissions from $Er^{3+}$, $Ho^{3+}$, and $Tm^{3+}$ dopants, respectively, in $KMnF_3$ nanoparticles by a novel oil-based procedure.[36] In our case, a similar situation for the effects of the $Mn^{2+}$ cations on the red to green intensity ratio occurred in cube $NaYF_4$:$Mn^{2+}/Yb^{3+}/Er^{3+}$ (Figure 5a and b). However, the red to green intensity ratio of $Er^{3+}$ emission bands can not nearly be tuned in hexagonal $NaYF_4$:Yb/Er microtubes by adding $Mn^{2+}$ content (Figure 5d and e), indicating a void energy transfer between $Er^{3+}$ and

$Mn^{2+}$. The tunable emission can be obtained in hexagonal $NaYF_4$:Yb/Er by adding Yb content (Figure 5c, e-g). It is well known that upconversion emission characters were sensitive to crystallite size, the concentration and distribution of dopant in solid solution.[54] The red to green intensity ratio from hexagonal $NaYF_4$ are independent on the concentration of $Mn^{2+}$ dopant which may indicate that a low concentration or heterogeneous distribution of $Mn^{2+}$ dopants in hexagonal $NaYF_4$ solid solution.

To gain insights into the energy transfer process between the $Er^{3+}$ and $Mn^{2+}$, 532 nm photons directly excited into the $^2H_{11/2}$ green luminescence level of $Er^{3+}$ to assure the same population process of green luminescence level in a series of $NaYF_4$ microcrystals doubly doped with $Mn^{2+}$ and $Er^{3+}$. The down-conversion spectra from in $NaYF_4$:$Mn^{2+}/Er^{3+}$ microcrystals with the different $Mn^{2+}$ concentrations and hydrothermal reaction time are shown in Figure 6. By comparing the



**Figure 6.** Downconversion emission spectra of $NaYF_4$:Er (1 mol %) products obtained at 200 °C as a function of hydrothermal reaction time and concentration of $Mn^{2+}$ dopant. All the samples are measured under the same conditions with 532 nm laser as excitation source operating at 300 mW.

luminescence spectra, the intensity ratio for red to green emission prominently increases with the doping concentration of $Mn^{2+}$ rise, which is consistent with the literature report.[55] Noted that single-band red downconversion emission can be obtained due to the extremely efficient resonance exchange-energy transfer process between the $Mn^{2+}$ and $Er^{3+}$ levels[30] in $\alpha$-$NaYF_4$:$Mn^{2+}$(30 mol %)/$Er^{3+}$(1.0 mol %) nanoparticles under 532 nm photon excitation, which enables them to serve as novel downconversion materials for solar cell.[56] While the intensity ratio for red to green spectra prominently decreases with reaction time prolonging, which is attributed to a more ineffective energy transfer between $Er^{3+}$ and $Mn^{2+}$. The proposed downconversion mechanism is indicated in Figure S10. Noted that nonradiative relaxation of Er:$^4S_{3/2} \rightarrow ^4F_{9/2}$ is not responsible for the population of $^4F_{9/2}$ level due to the low phonon energy, which is testified by the absence of red fluorescence in $NaYF_4$ microtubes singly doped with $Er^{3+}$ in Figure 6.

To further verify the motivation of the ratio for red to green spectra adjusted by reaction time, we carefully compared the XRD for a series of $NaYF_4$ samples singly doped with 30 mol % $Mn^{2+}$ obtained at different reaction time in Figure S11. We amazedly find that the shift of peaks gradually reduces with the

extension of reaction time. Therefore, we speculated that content of $Mn^{2+}$ is gradually lowered, which may derive from the outward migration of $Mn^{2+}$ defects with extension of reaction time. This speculation is further support by the result of EDX of the 30 % Mn-doped $NaYF_4$ samples (Figure S12). Finally, residual $Mn^{2+}$ may mainly distribute on the surface of final microcrystal particles by the outward migration of defects. The lower concentration and local distribution should be account for ineffective energy transfer between $Er^{3+}$ and $Mn^{2+}$. This kind of self purification process of the matrix, by $Mn^{2+}$ interstitial migration from inner to outer, is beneficial to the formation of the hollow structure. More interestingly, the shift of (111) peak originated from the cubic phase is bigger than that of (110) peak derived from the hexagonal phase in Figure S11b and c, suggesting that $Mn^{2+}$ ions prefer to doped into cubic phase $NaYF_4$ than hexagonal phase $NaYF_4$.

## ■ CONCLUSION

In summary, we reveal the specific roles of $Mn^{2+}$ dopant in hydrothermal route to form uniform hollow bundle-shaped $\beta$-$NaYF_4$ microtubes through a series of controlled experiments. The mechanisms of morphology evolution controlled by $Mn^{2+}$ dopant for uniform bundle-shaped microtube based on the enhanced Ostwald-ripening process and single source supply of $\alpha$-phase precursor particles, by delaying the process of crystal phase transition and implanting defects, are proposed. This significantly refined understanding allows us to develop an efficient and highly reproducible process for creating the hollow structure materials. The different distinctive morphologies including bundle-shaped microtubes, prismatic microtubes, prismatic short rods, thin plates and particles can also be obtained by adjusting the ratio of $Mn^{2+}$ to $RE^{3+}$, the amount of trisodium citrate and the pH values in the mother solution. Importantly, $Mn^{2+}$ doped $NaYF_4$:$Er^{3+}$/$Yb^{3+}$ samples including cube phase nanoparticles and hexagonal phase bundle-shaped microtubes show the intense upconversion and downconversion output. In addition to, by varying concentration of the $Mn^{2+}$ or $Yb^{3+}$ ions, the red to green upconversion intensity ratio of $\alpha$-$NaYF_4$ nanoparticles can be deliberated tuning, but $\beta$-microtubes with tuning of the output color are only obtained by adjusting concentration of $Yb^{3+}$ ions. These results of upconversion spectra indicate that the distribution and the concentration of $Mn^{2+}$ in solid solution have been modified in a phase transition and growth process. This speculation is further support by some measurement results of downconversion spectra, EDX and XRD. Therefore, up and downconversion spectroscopy can be applied to verify the local distribution variation of dopant ions in matrix. We believe that the size- and phase-controlled high-quality $NaYF_4$:$Yb^{3+}$/$Er^{3+}$ nano/microcrystals with the tunable output color are good candidate materials for many applications such as lasers, displays, solar cell, imaging, and biosensing, and the unique Ostwald ripening pathway may provide a versatile approach for fabricating a wide range of hollow nano/microcrystals.

## ■ ASSOCIATED CONTENT

**Ⓢ Supporting Information**

XRD patterns (Figures S1, S2, S3, S5, S8, S11), SEM images (Figures S2, S4, S6, S7), EDX pattern (Figure S12), and the energy level diagrams of the $Mn^{2+}$, $Er^{3+}$ and $Yb^{3+}$ (Figures S9, S10). This material is available free of charge via the Internet at http://pubs.acs.org.

## ■ AUTHOR INFORMATION

**Corresponding Author**

*E-mail: gaodangli@163.com.

**Author Contributions**

The manuscript was written through contributions of all authors. All authors have given approval to the final version of the manuscript.

**Notes**

The authors declare no competing financial interest.

## ■ ACKNOWLEDGMENTS

## ■ REFERENCES

(1) Yin, Y. D.; Rioux, R. M.; Erdonmez, C. K.; Hughes, S.; Somorjai, G. A.; Alivisatos, A. P. *Science* **2004**, *304*, 711−714.

(2) Zhang, F.; Shi, Y. F.; Sun, X. H.; Zhao, D. Y.; Stucky, G. D. *Chem. Mater.* **2009**, *21*, 5237−5243.

(3) Xiao, G.; Zeng, Y.; Jiang, Y.; Ning, J.; Zheng, W.; Liu, B.; Chen, X.; Zou, G.; Zou, B. *Small* **2013**, *9*, 793−799.

(4) El Mel, A. A.; Buffière, M.; Tessier, P. Y.; Konstantinidis, S.; Xu, W.; Du, K.; Wathuthanthri, I.; Choi, C. H.; Bittencourt, C.; Snyders, R. *Small* **2013**, *7*, 2838−2843.

(5) Shan, J. N.; Yao, N.; Ju, Y. G. *J. Nanopart. Res.* **2010**, *12*, 1429−1438.

(6) Cheng, Y.; Wang, Y. S.; Zheng, Y. H.; Qin, Y. *J. Phys. Chem. B* **2005**, *109*, 11548−11551.

(7) Chen, Z. M.; Geng, Z. R.; Shi, M. L.; Liu, Z. H.; Wang, Z. L. *CrystEngComm* **2009**, *11*, 1591−1596.

(8) Zhang, H. G.; Zhu, Q. S.; Zhang, Y.; Wang, Y.; Zhao, L.; Yu, B. *Adv. Funct. Mater.* **2007**, *17*, 2766−2771.

(9) Lou, X. W.; Wang, Y.; Yuan, C. L.; Lee, J. Y.; Archer, L. A. *Adv. Mater.* **2006**, *18*, 2325−2329.

(10) Qiao, R.; Zhang, X. L.; Qiu, R.; Kim, J. C.; Kang, Y. S. *Chem.—Eur. J.* **2009**, *15*, 1886−1892.

(11) Liu, B.; Zeng, H. C. *Small* **2005**, *1*, 566−571.

(12) Tian, X. L.; Li, J.; Chen, K.; Han, J.; Pan, S. L. *Cryst. Growth Des.* **2009**, *9*, 4927−4932.

(13) Wang, X.; Zhuang, J.; Peng, Q.; Li, Y. D. *Inorg. Chem.* **2006**, *45*, 6661−6665.

(14) Zhou, K. B.; Wang, X.; Sun, X. M.; Peng, Q.; Li, Y. D. *J. Catal.* **2005**, *229*, 206−212.

(15) Lu, H. C.; Yi, G. S.; Zhao, S. Y.; Chen, D. P.; Guo, L. H.; Cheng, J. *J. Mater. Chem.* **2004**, *14*, 1336−1341.

(16) Sivakumar, S.; Diamente, P. R.; van Veggel, F. C. J. M. *Chem.—Eur. J.* **2006**, *12*, 5878−5884.

(17) Wang, L. Y.; Yan, R. X.; Huo, Z. Y.; Wang, L.; Zeng, J. H.; Bao, J.; Wang, X.; Peng, Q.; Li, Y. D. *Angew. Chem., Int. Ed.* **2005**, *44*, 6054−6057.

(18) Kramer, K. W.; Biner, D.; Frei, G.; Gudel, H. U.; Hehlen, M. P.; Luthi, S. R. *Chem. Mater.* **2004**, *16*, 1244−1244.

(19) Sun, Y. J.; Chen, Y.; Tian, L. J.; Yu, Y.; Kong, X. G.; Zhao, J. W.; Zhang, H. *Nanotechnology* **2007**, *18*, 275609.

(20) Wang, F.; Han, Y.; Lim, C. S.; Lu, Y. H.; Wang, J.; Xu, J.; Chen, H. Y.; Zhang, C.; Hong, M. H.; Liu, X. G. *Nature* **2010**, *463*, 1061−1065.

(21) Zhang, F.; Wan, Y.; Yu, T.; Zhang, F. Q.; Shi, Y. F.; Xie, S. H.; Li, Y. G.; Xu, L.; Tu, B.; Zhao, D. Y. *Angew. Chem.* **2007**, *119*, 8122−8125.

(22) Li, C. X.; Yang, J.; Quan, Z. W.; Yang, P. P.; Kong, D. Y.; Lin, J. *Chem. Mater.* **2007**, *19*, 4933−4942.

(23) Wang, X.; Li, Y. D. *Chem.—Eur. J.* **2003**, *9*, 5627−5635.

(24) Zhuang, J. L.; Liang, L. F.; Sung, H. H. Y.; Yang, X. F.; Wu, M. M.; Williams, I. D.; Feng, S. H.; Su, Q. *Inorg. Chem.* **2007**, *46*, 5404−5410.

(25) Gao, D. L.; Zhang, X. Y.; Gao, W. *J. Appl. Phys.* **2012**, *111*, 033505.

(26) Shan, J. N.; Uddi, M.; Wei, R.; Yao, N.; Ju, Y. G. *J. Phys. Chem. C* **2010**, *114*, 2452−2461.

(27) Yang, J. P.; Shen, D. K.; Li, X. M.; Li, W.; Fang, Y.; Wei, Y.; Yao, C.; Tu, B.; Zhang, F.; Zhao, D. Y. *Chem.—Eur. J.* **2012**, *18*, 13642−13650.

(28) Yu, X. F.; Li, M.; Xie, M. Y.; Chen, L. D.; Li, Y.; Wang, Q. Q. *Nano Res.* **2010**, *3*, 51−60.

(29) Chen, D. Q.; Huang, P.; Yu, Y. L.; Huang, F.; Yang, A. P.; Wang, Y. S. *Chem. Commun.* **2011**, *47*, 5801−5803.

(30) Tian, G.; Gu, Z. J.; Zhou, L. J.; Yin, W. Y.; Liu, X. X.; Yan, L.; Jin, S.; Ren, W. L.; Xing, G. M.; Li, S. J.; Zhao, Y. L. *Adv. Mater.* **2012**, *24*, 1226−1231.

(31) Dou, Q. Q.; Zhang, Y. *Langmuir* **2011**, *27*, 13236−13241.

(32) Yang, L. W.; Li, Y.; Li, Y. C.; Li, J. J.; Hao, J. H.; Zhong, J. X.; Chu, P. K. *J. Mater. Chem.* **2012**, *22*, 2254−2262.

(33) Kramers, H. A. *Physica* **1940**, *4*, 284−304.

(34) Voß, B.; Nordmann, J.; Uhl, A.; Komban, R.; Haase, M. *Nanoscale* **2013**, *5*, 806−812.

(35) Sarkar, S.; Meesaragandla, B.; Hazra, C.; Mahalingam, V. *Adv. Mater.* **2013**, *25*, 856−860.

(36) Wang, J.; Wang, F.; Wang, C.; Liu, Z.; Liu, X. G. *Angew. Chem., Int. Ed.* **2011**, *50*, 10369−10372.

(37) Xie, M. Y.; Peng, X. N.; Fu, X. F.; Zhang, J. J.; Li, G. L.; Yu, X. F. *Scr. Mater.* **2009**, *60*, 190−193.

(38) Talapin, D.; Rogach, A.; Haase, M.; Weller, H. *J. Phys. Chem. B* **2001**, *105*, 12278.

(39) Liang, X.; Wang, X.; Zhuang, J.; Peng, Q.; Li, Y. D. *Adv. Funct. Mater.* **2007**, *17*, 2757−2765.

(40) Sugimoto, T. *Adv. Colloid Interface Sci.* **1987**, *28*, 65−108.

(41) Clark, M. D.; Kumar, S. K.; Owen, J. S.; Chan, E. M. *Nano Lett.* **2011**, *11*, 1976−1980.

(42) Carp, O.; Huisman, C. L.; Reller, A. *Prog. Solid State Chem.* **2004**, *32*, 33−177.

(43) Kitiyanan, A.; Ngamsinlapasathian, S.; Pavasupree, S.; Yoshikawa, S. *Solid State Chem.* **2005**, *178*, 1044−1048.

(44) Durr, M.; Rosselli, S.; Yasuda, A.; Nelles, G. *J. Phys. Chem. B* **2006**, *110*, 21899−21902.

(45) Chen, D. Q.; Yu, Y. L.; Huang, F.; Wang, Y. S. *Chem. Commun.* **2011**, *47*, 2601−2603.

(46) Filankembo, A.; Pileni, M. P. *J. Phys. Chem. B* **2000**, *104*, 5865−5868.

(47) Lu, H. B.; Wang, S. M.; Zhao, L.; Dong, B. H.; Xu, Z. X.; Li, J. C. *RSC Adv.* **2012**, *2*, 3374−3378.

(48) Zhang, F.; Zhao, D. Y. *ACS Nano* **2009**, *3*, 159−164.

(49) Wang, F.; Liu, X. G. *J. Am. Chem. Soc.* **2008**, *130*, 5642−5643.

(50) Gao, D. L.; Zhang, X. Y.; Zheng, H. R.; Gao, W.; He, E. J. *J. Alloys Compd.* **2013**, *554*, 395−399.

(51) Sarkar, S.; Hazra, C.; Mahalingam, V. *Dalton Trans.* **2013**, *42*, 63−66.

(52) Sheng, J.; Tang, K. B.; Su, D.; Zeng, S. Y.; Qi, Y. X.; Zheng, H. G. *J. Fluorine Chem.* **2009**, *130*, 742−748.

(53) Zhang, Y.; Lin, J. D.; Vijayaragavan, V.; Bhakoo, K. K.; Tan, T. T. Y. *Chem. Commun.* **2012**, *48*, 10322−10324.

(54) Gao, D. L.; Zhang, X. Y.; Zheng, H. R.; Shi, P.; Li, L.; Ling, Y. W. *Dalton Trans.* **2013**, *42*, 1834−1841.

(55) He, E. J.; Zheng, H. R.; Gao, W.; Tu, Y. X.; Lu, Y.; Tian, H. N.; Li, G. A. *J. Nanosci. Nanotechol.* **2013**, DOI: 10.1166/jnn.2013.8040.

(56) Gao, D. L.; Zheng, H. R.; Zhang, X. Y.; Fu, Z. X.; Zhang, Z. L.; Tian, Y.; Cui, M. *Appl. Phys. Lett.* **2011**, *98*, 011907.